

**GeSn FILM DEPOSITED BY RF MAGNETRON  
SPUTTERING FOR PHOTODETECTOR  
APPLICATIONS**

**HADI MAHMODI SHEIKH SARMAST**

**UNIVERSITI SAINS MALAYSIA**

**2017**

**GeSn FILM DEPOSITED BY RF MAGNETRON  
SPUTTERING FOR PHOTODETECTOR  
APPLICATIONS**

by

**HADI MAHMODI SHEIKH SARMAST**

**Thesis submitted in fulfillment of the requirements  
for the degree of  
Doctor of Philosophy**

**July 2017**

## ACKNOWLEDGEMENT

Firstly, I would like to express my sincere gratitude to my supervisor, Professor Dr. Md Roslan Hashim, for the continuous support of my Ph.D study and related research, for his patience, motivation, and immense knowledge. I benefited a lot from his valuable guidance, not only in the direction of research, but also in my method of research, which for me was often of greater importance.

I take this unique opportunity to thank School of Physics, for providing me the necessary facilities, an excellent academic environment for a successful completion of my work and Research Grant (1001/PFIZIK/846072) for supporting this work.

I would also like to express my appreciation to the laboratory assistants in the Nano-Optoelectronics Research Laboratory (NORLAB) for their co-operation, technical assistance, and valuable contribution to my work. The assistance from the staff of the Solid-State Physics Laboratory is also acknowledged.

Ultimately, it is the encouragement, understanding, and support of my family, which provided me the courage to embark in this venture. I would like to thank my wife for giving me their great love, endless support, sympathy and encouragement when I needed it.

Finally, I offer my regards and blessings to all of those who supported me in any respect during the completion of the project.

Hadi Mahmodi Sheikh Sarmast

July 2017

## TABLE OF CONTENTS

<b>ACKNOWLEDGEMENT</b>	ii
<b>TABLE OF CONTENTS</b>	iii
<b>LIST OF TABLES</b>	viii
<b>LIST OF FIGURES</b>	xi
<b>LIST OF SYMBOLS</b>	xvii
<b>LIST OF ABBREVIATIONS</b>	xx
<b>ABSTRAK</b>	xxii
<b>ABSTRACT</b>	xxiv
<b>CHAPTER 1: INTRODUCTION</b>	1
1.1 Introduction	1
1.2 Problem Statement	3
1.3 Research Objectives	5
1.4 Scope of Research	5
1.5 Outline of Thesis	6
<b>CHAPTER 2: LITERATURE REVIEW AND THEORY</b>	8
2.1 Introduction	8
2.2 Fundamentals of Germanium Tin Alloy	8
2.2.1 Alloy Formation Mechanism	12
2.3 Overview and Background of $\text{Ge}_{1-x}\text{Sn}_x$ Growth Techniques	13
2.3.1 CVD	15
2.3.2 MBE	16
2.3.3 Sputtering	17
2.3.4 Laser Synthesis	18

2.4	Semiconductor Thin Films	19
2.4.1	Physical Vapor Deposition	20
2.5	Sputter Deposition Technique	22
2.5.1	Theory of Sputter Deposition	22
2.5.2	Alloy Sputtering	24
2.5.3	Sputtering System	25
2.5.4	RF Diode Sputtering	26
2.5.5	Magnetron Sputtering	26
2.5.6	Sputtering Parameters	27
2.6	Post-deposition Annealing	28
2.7	Overview of Semiconductor Photodetectors	30
2.8	Principle of Photodetector Device	32
2.8.1	Photodetection Principle	33
2.8.2	Metal-Semiconductor-Metal Photodetector	34
2.9	Summary	35
<b>CHAPTER 3: METHODOLOGY</b>		36
3.1	Introduction	36
3.2	Growth of $\text{Ge}_{1-x}\text{Sn}_x$ Alloy	36
3.2.1	Sample Preparation	36
3.2.2	RF Magnetron Sputtering of $\text{Ge}_{1-x}\text{Sn}_x$ Thin Films	38
3.2.3	Rapid Thermal Annealing of $\text{Ge}_{1-x}\text{Sn}_x$ Films	39
3.3	Fabrication of MSM Photodetector	42
3.3.1	Metal Coating Tool: Vacuum Thermal Evaporation	43
3.3.2	Thermal Annealing Process: Tube Furnace	44
3.4	Principles of the Characterization Tools	45

3.4.1	The Structural Properties Tools	45
3.4.1(a)	Field Emission Scanning Electron Microscope (FESEM)	45
3.4.1(b)	Atomic Force Microscope (AFM)	46
3.4.1(c)	X-ray Diffraction (XRD)	48
3.4.1(d)	Energy-dispersive X-ray Spectroscopy (EDX)	51
3.4.1(e)	X-ray Photoelectron Spectroscopy (XPS)	52
3.4.2	The Optical Characterization Tools	54
3.4.2(a)	Raman Spectroscopy	54
3.4.2(b)	UV-Vis-NIR Spectroscopy	57
3.4.3	Electrical Characterization	59
3.5	Summary	60
<b>CHAPTER 4: THE STUDY OF AMORPHOUS SPUTTERED Ge<sub>1-x</sub>Sn<sub>x</sub> ALLOY</b>		62
4.1	Introduction	62
4.2	Ge <sub>1-x</sub> Sn <sub>x</sub> Co-Sputtering on Si Substrate: The Effect of Post Deposition Annealing	62
4.2.1	Energy-dispersive X-ray (EDX) Spectroscopy	63
4.2.2	Field Emission Scanning Electron Microscopy	65
4.2.3	Atomic Force Microscopy	67
4.2.4	Raman Analysis	68
4.2.5	Amorphous GeSn MSM Photodetector	72
4.3	Ge <sub>1-x</sub> Sn <sub>x</sub> Co-Sputtering on Glass Substrate	76
4.3.1	Energy Dispersive X-ray (EDX) Spectroscopy	77
4.3.2	Atomic Force Microscopy	77
4.3.3	Raman Analysis	79

4.3.4	Optical Properties	81
4.4	Summary	84
<b>CHAPTER 5: THE STUDY OF NANOCRYSTALLINE CO-SPUTTERED <math>\text{Ge}_{1-x}\text{Sn}_x</math> ALLOY ON Si SUBSTRATE</b>		87
5.1	Introduction	87
5.2	$\text{Ge}_{1-x}\text{Sn}_x$ Co-sputtering on Si Substrate (The Influence of Substrate Temperature)	87
5.2.1	Energy-dispersive X-ray Spectroscopy	88
5.2.2	Field emission scanning electron microscopy	89
5.2.3	Atomic Force Microscopy	92
5.2.4	Raman Analysis	94
5.2.5	X-ray Photoelectron Spectroscopy (XPS)	97
5.2.6	XRD Analysis	99
5.3	Rapid Thermal Annealing of Co-sputtered $\text{Ge}_{1-x}\text{Sn}_x$ Alloy	100
5.3.1	Field Emission Scanning Electron Microscopy	100
5.3.2	Energy-Dispersive X-ray Spectroscopy	102
5.3.3	Atomic Force Microscopy	104
5.3.4	Raman Analysis	105
5.3.5	XRD Analysis	108
5.3.6	Nanocrystalline $\text{Ge}_{1-x}\text{Sn}_x$ MSM Photodetector	111
5.4	Summary	117
<b>CHAPTER 6: NANOCRYSTALLINE <math>\text{Ge}_{1-x}\text{Sn}_x</math> GROWTH: ANNEALING MULTILAYER Ge-Sn-Ge</b>		119
6.1	Introduction	119
6.2	Rapid Thermal Treatment of Sputter-deposited Multilayer Ge-Sn-Ge	119
6.3	The Effect of Thermal Treatment Temperature	121

6.3.1	Field Emission Scanning Electron Microscopy	121
6.3.2	Energy-Dispersive X-ray Spectroscopy	124
6.3.3	Atomic Force Microscopy	125
6.3.4	Raman Analysis	126
6.3.5	X-ray Photoemission Spectroscopy (XPS)	131
6.3.6	XRD Analysis	132
6.3.7	Electrical Characterization of $\text{Ge}_{1-x}\text{Sn}_x$ MSM Photodetector	135
6.4	Summary	137
<b>CHAPTER 7: CONCLUSIONS AND FUTURE WORKS</b>		139
<b>REFERENCES</b>		142
<b>APPENDICES</b>		159
<b>LIST OF PUBLICATIONS</b>		167



## LIST OF TABLES

		Page
Table 2.1	Electron and hole mobility of group IV semiconductors.	11
Table 2.2	Fabricated various photodetector on $\text{Ge}_{1-x}\text{Sn}_x$ .	31
Table 4.1	The deposition parameters of the $\text{Ge}_{1-x}\text{Sn}_x$ alloy by RF magnetron sputtering.	63
Table 4.2	The Ge, Sn, and O atomic concentration of as-sputtered $\text{Ge}_{1-x}\text{Sn}_x$ sample and annealed samples at various temperature for 30 minutes.	64
Table 4.3	The RMS surface roughness of as-sputtered and annealed thin films.	68
Table 4.4	The details of the Ge-Ge mode of Raman spectra for the as-sputtered and annealed samples. The frequency shift value is compared to the as-sputtered sample.	70
Table 4.5	Schottky barrier height ( $\phi_B$ ) and ideality factor ( $n$ ) of photodetectors.	75
Table 4.6	The deposition parameters of the co-sputtered $\text{Ge}_{1-x}\text{Sn}_x$ layers on the glass substrate.	76
Table 4.7	The atomic Sn and Ge concentration in the a- $\text{Ge}_{1-x}\text{Sn}_x$ alloy films.	77
Table 4.8	The details of the Ge-Ge mode of Raman spectra for $\text{Ge}_{1-x}\text{Sn}_x$ samples. The frequency shift value is compared to the Ge sample.	80
Table 4.9	Optical band gap of the Ge and $\text{Ge}_{1-x}\text{Sn}_x$ thin films sputtered on glass substrate.	84

Table 5.1	The deposition parameters of the $\text{Ge}_{1-x}\text{Sn}_x$ alloy on Si substrate at different substrate temperature.	88
Table 5.2	The Ge and Sn atomic concentration of $\text{Ge}_{1-x}\text{Sn}_x$ sample sputtered at various substrate temperatures.	89
Table 5.3	The surface RMS roughness of the sputtered $\text{Ge}_{1-x}\text{Sn}_x$ samples at different substrate temperature.	93
Table 5.4	The Ge-Ge phonon modes detected in Raman spectra of $\text{Ge}_{1-x}\text{Sn}_x$ films sputtered at various substrate temperatures. The frequency shift value is compared to the RT sputtered sample.	95
Table 5.5	The Ge and Sn atomic concentration of the as-sputtered sample and annealed samples at various temperature ( $\text{Ge}_{1-x}\text{Sn}_x$ ).	103
Table 5.6	The RMS surface roughness of as-sputtered and rapid thermal annealed thin films.	105
Table 5.7	The details of the Ge-Ge mode of Raman spectra for as-sputtered and annealed $\text{Ge}_{1-x}\text{Sn}_x$ samples. The frequency shift value is compared to the as-sputtered sample.	106
Table 5.8	The XRD data for the $\text{Ge}_{1-x}\text{Sn}_x$ samples at different annealing temperatures.	109
Table 5.9	Lattice spacing (d-spacing), lattice constants (a), calculated strain values, and mismatch determined for the annealed GeSn samples with different annealing temperatures. The mismatch is between GeSn thin film and Si substrate.	111
Table 5.10	Schottky barrier height ( $\phi_B$ ) and ideality factor ( $n$ ) of GeSn based MSM photodetectors.	114
Table 5.11	The response and recovery time of the MSM Photodetectors.	117

Table 6.1	The deposition parameters of the multilayer Ge-Sn sputtering.	120
Table 6.2	The Ge, Sn, Si and O concentrations of all the samples.	125
Table 6.3	The surface RMS roughness of the as-sputtered multilayer annealed structures and at different annealing temperature.	126
Table 6.4	The details of the Ge-Ge mode of Raman spectra for as-sputtered and annealed $\text{Ge}_{1-x}\text{Sn}_x$ samples. The frequency shift value is compared to the as-sputtered sample.	129
Table 6.5	The XRD data for the annealed multilayer Ge-Sn-Ge samples at different temperatures.	133

## LIST OF FIGURES

		<b>Page</b>
Figure 2.1	Equilibrium phase diagram of Ge-Sn. Shown is the Ge rich side up to 15% Sn [28].	9
Figure 2.2	The energy separation between the L-point of the Brillouin zone ( $E_{cL}$ ) and local minimum at the $\Gamma$ -point ( $E_{c\Gamma}$ ).	10
Figure 2.3	Direct and indirect bandgaps of unstrained $\text{Ge}_{1-x}\text{Sn}_x$ alloys as a function of $\alpha$ -Sn concentration [50].	10
Figure 2.4	Absorption coefficient of $\text{Ge}_{1-x}\text{Sn}_x$ with 4.5% Sn and Ge formed by solid phase epitaxy on silicon, measured by spectroscopic ellipsometry.	12
Figure 2.5	(a) Vacancy diffusion, and (b) interstitial diffusion.	13
Figure 2.6	Timeline of GeSn epitaxy providing an overview of important achievements since $\text{Ge}_{1-x}\text{Sn}_x$ has been mentioned for the first time as possible direct bandgap material in 1982.	14
Figure 2.7	The Schematic diagram of the PVD main steps.	21
Figure 2.8	Sputtering process shows the ion bombardment of the target surface.	23
Figure 2.9	The schematic shown of multi-target sputtering.	25
Figure 2.10	The schematic diagram of magnetron sputtering.	27
Figure 2.11	Photonic excitation in a semiconductor.	33
Figure 2.12	The schematic shown of (a) MSM photodetector, and (b) its cross-section view showing the electric field distribution.	35
Figure 3.1	Flow chart of the current research work: Methodology and fabrication process.	37
Figure 3.2	(a) Image of the RF magnetron sputtering system, and (b) the schematic diagram of targets and substrate configuration.	39
Figure 3.3	(a) Rapid thermal process system. (b) The schematic diagram of RTA system.	40

Figure 3.4	Temperature profile in rapid-thermal annealing process.	41
Figure 3.5	(a) Schematic of the metal contact for MSM PD fabrication. (b) Deposited metal contacts on the $\text{Ge}_{1-x}\text{Sn}_x$ thin films on Si substrate.	42
Figure 3.6	(a) Schematic diagram of vacuum thermal evaporation system. (b) Image of the vacuum thermal evaporation system in NOR Lab.	43
Figure 3.7	(a) Schematic diagram of thermal annealing furnace. (b) The used tube furnace in NOR Lab.	44
Figure 3.8	The FEI Nova NanoSEM 450 FESEM.	46
Figure 3.9	(a) The schematic of AFM system that shows the cantilever and tip. (b) The Dimension EDGE- BRUKER AFM system.	47
Figure 3.10	Schematic of collisions between X-Ray beams and the atoms arranged in the crystal lattice planes.	49
Figure 3.11	Image of the high-resolution XRD equipment.	51
Figure 3.12	Rough schematic of XPS physics - Photoelectric Effect [135]	53
Figure 3.13	The XPS system in SERC center used in this project.	54
Figure 3.14	The typical Raman spectrum that shows Raman characteristics.	55
Figure 3.15	The schematic show of FWHM and HWHM for Raman peak.	56
Figure 3.16	Raman system in NOR Lab.	57
Figure 3.17	UV-Vis-NIR spectrophotometer (Agilent, Cary 5000).	58
Figure 3.18	Semiconductor Characterization System (Keithley 4200-SCS).	59
Figure 3.19	(a) The Xenon lamp and monochromator system for measuring the spectral responsivity. (b) The front view of the monochromator.	60
Figure 4.1	The typical EDX spectra of the $\text{Ge}_{1-x}\text{Sn}_x$ thin film of the as-sputtered sample acquired at 10 kV.	64

Figure 4.2	FESEM images of the $\text{Ge}_{1-x}\text{Sn}_x$ thin films sputtered on the n-Si (100) substrate (a) as-sputtered sample and annealed for 30 min at (b) 200 °C, (c) 300 °C, (d) 400 °C and (e) 500 °C.	65
Figure 4.3	Cross-sectional view of FESEM image of the as-sputtered sample.	66
Figure 4.4	AFM images of the $\text{Ge}_{1-x}\text{Sn}_x$ thin films sputtered on the n-Si (100) substrate (a) as-sputtered sample and annealed for 30 min at (b) 200 °C, (c) 300 °C, (d) 400 °C and (e) 500 °C.	67
Figure 4.5	Raman spectra obtained from the $\text{Ge}_{1-x}\text{Sn}_x$ thin films before annealing (as-sputtered) and after annealing at 200 °C, 300 °C, 400 °C, and 500 °C.	69
Figure 4.6	Current-voltage characteristics of the fabricated MSM photodetectors on the as-sputtered and annealed sample at 200 °C, 300 °C and 400 °C measured in dark ( $I_{\text{dark}}$ ) and under illumination ( $I_{\text{photo}}$ ).	72
Figure 4.7	The Schottky behavior show in the range of -1 V to 1 V for MSM photodetector.	73
Figure 4.8	The current gain of the $\text{Ge}_{1-x}\text{Sn}_x$ photodetectors on the as-sputtered and annealed samples at 200 °C, 300 °C and 400 °C.	74
Figure 4.9.	The three-dimensional atomic force microscopy images of the (a) Ge and $\text{Ge}_{1-x}\text{Sn}_x$ thin films with various Sn content: (b) 11.20 at%, (c) 13.61 at%, and (d) 16.44 at%.	78
Figure 4.10	The Raman spectra of (a) Ge sample and a- $\text{Ge}_{1-x}\text{Sn}_x$ thin films with different Sn content: (b) 11.20 at%, (c) 13.61 at%, and (d) 16.55 at%.	79
Figure 4.11	Transmission spectra of the Ge and $\text{Ge}_{1-x}\text{Sn}_x$ thin films sputtered on glass substrate.	82
Figure 4.12	Absorption coefficient of the Ge and $\text{Ge}_{1-x}\text{Sn}_x$ thin films sputtered on glass substrate versus photon energy.	83
Figure 4.13	$(\alpha\hbar\omega)^{1/2}$ as a function of photon energy for the a- $\text{Ge}_{1-x}\text{Sn}_x$ thin films with different Sn content.	84
Figure 5.1	The typical EDX spectra of the $\text{Ge}_{1-x}\text{Sn}_x$ thin film of as-sputtered sample acquired at 10 kV.	89

Figure 5.2	The FESEM images of the $\text{Ge}_{1-x}\text{Sn}_x$ alloy films sputtered at various substrate temperatures.	90
Figure 5.3	The cross-sectional view of the sputtered $\text{Ge}_{1-x}\text{Sn}_x$ thin films on Si substrate at different substrate temperature.	91
Figure 5.4	Three-dimensional AFM images of the co-sputtered $\text{Ge}_{1-x}\text{Sn}_x$ thin films at different substrate temperatures: RT, 140 °C, 160 °C, 180 °C, 200 °C.	93
Figure 5.5	Raman spectra of the (a) RT sputtered GeSn thin films and elevated temperature sputtered films at (b) 140 °C, (c) 160 °C, (d) 180, and (e) 200 °C.	95
Figure 5.6	FWHM and surface roughness of the sputtered $\text{Ge}_{1-x}\text{Sn}_x$ films at different deposition temperatures.	97
Figure 5.7	XPS spectra of the sputtered GeSn film at 140 °C. (a) Ge and GeO peak, and (b) Sn peak.	98
Figure 5.8	X-ray diffraction (XRD) spectra of $\text{Ge}_{1-x}\text{Sn}_x$ alloy sputtered at different substrate temperature: (a) RT, (b) 140 °C, (c) 160 °C, (d) 180 °C, and (e) 200 °C.	99
Figure 5.9	FESEM images of (a) the as-sputtered and rapid thermal annealed samples at (b) 350 °C, (c) 400 °C and (d) 450 °C.	101
Figure 5.10	Cross-sectional FESEM images of the as-sputtered and annealed thin films at (b) 350 °C, (c) 400 °C and (d) 450 °C.	102
Figure 5.11	The typical EDX spectra of the $\text{Ge}_{1-x}\text{Sn}_x$ thin film, which belongs to the as-sputtered sample acquired at 10 kV.	103
Figure 5.12	The three-dimensional AFM images of the as-sputtered sample ( $T_s = 140$ °C) and annealed samples at (b) 350 °C, (c) 400 °C and (d) 450 °C.	104
Figure 5.13	The Raman spectra of (a) as-sputtered sample and annealed samples at (b) 350 °C, (c) 400 °C, and (d) 450 °C. The inset shows the spectrum from a bulk n-Ge (100) wafer.	105
Figure 5.14	X-ray diffraction (XRD) spectra of (a) the as-sputtered $\text{Ge}_{1-x}\text{Sn}_x$ thin films on the Si substrate and rapid thermal annealed films at (b) 350 °C, (c) 400 °C, and (d) 450 °C.	108
Figure 5.15	Current-voltage characteristics of the fabricated MSM photodetectors on the sputtered $\text{Ge}_{1-x}\text{Sn}_x$ at $T_s=140$ °C and	112

	RTA annealed sample at 350 °C, 400 °C and 450 °C, measured in dark ( $I_{dark}$ ) and under illumination ( $I_{photo}$ ).	
Figure 5.16	Current gain of the fabricated MSM photodetectors on the sputtered $Ge_{1-x}Sn_x$ and 140 °C and RTA annealed sample at 350 °C, 400 °C and 450 °C.	113
Figure 5.17	The photo-response of the $Ge_{0.962}Sn_{0.038}$ MSM PD.	115
Figure 5.18	Photo-response of the as-sputtered sample at $T_s = 140$ °C and its RTA annealed one at 350 °C, 400 °C and 450 °C under illumination of on-off with a wavelength of 850 nm.	116
Figure 6.1	The schematic shown of multilayer Ge-Sn-Ge sputtered on Si substrate.	121
Figure 6.2	(a) The planar and (b) cross-sectional view of the as-sputtered multilayer Ge-Sn-Ge structure.	122
Figure 6.3	The planar view of the rapid thermal annealed multilayer samples: (a) 300 °C, (b) 350 °C, (c) 400 °C, and (d) 450 °C.	123
Figure 6.4	The cross-sectional view of the rapid thermal annealed multilayer samples: (a) 300 °C, (b) 350 °C, (c) 400 °C, and (d) 450 °C.	124
Figure 6.5	The typical EDX spectra of the $Ge_{1-x}Sn_x$ thin film, which belongs to the as-sputtered sample.	125
Figure 6.6	The three-dimensional AFM images of the (a) as-sputtered multilayer, and rapid thermal annealed multilayers: (b) 300 °C, (c) 350 °C, (d) 400 °C, and (e) 450 °C.	126
Figure 6.7	The Raman spectra of (a) as-sputtered sample and annealed samples at 300 °C, 350 °C, 400 °C, and 450 °C. The spectra have been offset for clarity.	127
Figure 6.8	Sn-Sn mode for the as-sputtered sample and RTA annealed at 300 °C, 350 °C, 400 °C and 450 °C.	128
Figure 6.9	Variation of Raman shift and FWHM of Ge-Ge peak versus annealing temperature.	130
Figure 6.10	XPS spectra of the annealed sample at 400 °C. (a) Ge and GeO peak, and (b) Sn peak.	131



Figure 6.11	X-ray diffraction (XRD) spectra of the rapid thermal annealed multilayers at 350 °C, 400 °C, and 450 °C.	132
Figure 6.12	Current-voltage characteristics of the fabricated MSM photodetectors on the RTA annealed sample at 400 °C, measured in dark ( $I_{dark}$ ) and under illumination ( $I_{Photo}$ ). The inset shows the current gain ( $I_{photo}/I_{dark}$ ).	125
Figure 6.13	The photo-response of the $\text{Ge}_{0.973}\text{Sn}_{0.027}$ MSM PD.	137

## LIST OF SYMBOLS

$a$	Lattice constant
$a_{Ge}$	Germanium lattice constant
$a_{Sn}$	Tin lattice constant
$a_0$	Stress-free lattice constant
$A$	Area
$A^{**}$	Richardson's constant
$b_{GeSn}$	Bowing parameter
$B$	Tauc constant
$d$	Interplanar spacing of the crystal planes
$D$	Average crystal size
$e$	Charge of electron
$E_c$	Conduction band
$E_{cL}$	Conduction band minimum at the L-point of the Brillouin zone
$E_{c\Gamma}$	Conduction band minimum at the $\Gamma$ -point of the Brillouin zone
$E_F$	Fermi level of semiconductor
$E_g$	Energy band gap
$E_g^{opt}$	Optical band gap
$E_v$	Valence band edge
$(hkl)$	Miller indices
$I$	Current
$I_{photo}$	Photo current
$I_{dark}$	Dark current

$I_0$	Saturation current
$J$	Current density
$k$	Boltzmann constant
$m_0$	Electron mass
$m^*$	Effective mass
$n$	Ideality factor
$\hbar$	Plank constant
$R$	Responsivity
$S$	Sensitivity
$t$	Time
$T$	Absolute temperature
$T_s$	Substrate/Deposition temperature
$V$	Voltage
$w$	Width
$X_{sn}$	Sn composition
$\alpha$	Absorption coefficient
$\beta$	FWHM of the diffraction peak
$\varepsilon_0$	Strain
$h\nu$	Photon energy
$\theta$	Incident / Diffraction angle
$X$	Semiconductor electron affinity
$\Phi$	Work function
$\varphi_B$	Schottky barrier height
$\Phi_M$	Metal work function
$\Phi_S$	Semiconductor work function

$\mu_n$       Electron mobility

$\mu_p$       Hole mobility

$\rho$         Resistivity

$\lambda$         Wavelength

$\lambda_c$       Light wavelength

## LIST OF ABBREVIATIONS

a.u.	Arbitrary unit
AFM	Atomic Force Microscopy
CVD	Chemical Vapor Deposition
DC	Direct Current
EDX	Energy Dispersive X-ray
eV	Electron volt
FESEM	Field Emission Scanning Electron Microscopy
FWHM	Full width at half maximum
HR-XRD	High resolution X-ray diffraction
HWHM	Half width at half maximum
GeSn	Germanium-Tin
I-V	Current-voltage
LO	Longitudinal optic
LPE	Liquid phase epitaxy
LT	Low temperature
MBE	Molecular Beam Epitaxy
MS	Metal-semiconductor
MSM	Metal-Semiconductor-Metal
NIR	Near-infrared
PD	Photodetector
PVD	Physical Vapor Deposition
PDA	Post-deposition annealing
RCA	Radio Corporation of America

RTA	Rapid thermal annealing
RTP	Rapid thermal process
RT	Room temperature
RMS	Root mean square
RF	Radio frequency
SBH	Schottky barrier height
SCCM	Standard cubic centimeters per minute
SEM	Scanning Electron Microscopy
SRH	Shockley-Read-Hall recombination
UHV	Ultra high vacuum
UHV-CVD	Ultra-high Vacuum Chemical Vapor Deposition
UV	Ultraviolet
UV-Vis-NIR	UV-visible-near infrared spectroscopy
VPE	Vapor phase epitaxy
$W_L$	Left width
$W_R$	Right width
XRD	X-ray diffraction
XPS	X-ray photoelectron spectroscopy

# **FILEM GeSn DIMENDAPKAN OLEH PERCIKAN MAGNETRON RF BAGI APLIKASI PENGESAN FOTO**

## **ABSTRAK**

Di dalam tesis ini, filem aloi semikonduktor  $\text{Ge}_{1-x}\text{Sn}_x$  telah disediakan melalui sistem percikan magnetron RF dalam usaha menumbuhkan filem pada suhu rendah untuk mengelakan pengasingan Sn pada permukaan. Sifat struktur, optik dan elektrik lapisan tersebut di atas substrat Si disiasat untuk aplikasi optoelektronik. Kajian terbahagi kepada tiga bahagian. Bahagian pertama kajian ini menjurus kepada kesan penyepuh-lindapan pasca-buang (PDA) untuk meningkatkan ciri-ciri optik dan elektrik lapisan nipis amorfus  $\text{Ge}_{1-x}\text{Sn}_x$  ke atas substrat Si (100). Sampel GeSn optima pada suhu penyepuh lindapan yang rendah iaitu pada 200 °C menunjukkan kekuatan phonon lebih tinggi, kekasaran permukaan terendah, dan prestasi elektrik yang baik. Diperhatikan bahawa jurang band optik lapisan GeSn ( $0.9 \text{ eV} < E_g < 1.05 \text{ eV}$ ) dikurangkan melalui peningkatan isi kandungan Sn dalam lapisan  $\text{Ge}_{1-x}\text{Sn}_x$  ke atas substrat kaca, yang mengubah jarak gelombang ke kawasan infra-merah (NIR). Dalam bahagian kedua kajian, lapisan nipis GeSn dipercik bersana pada subu substrat yang pelbagai ( $T_s$ ). Lapisan GeSn yang ddeposit pada  $T_s=140 \text{ °C}$  memaparkan pembentukan fasa kristal dengan orientasi (111). Sampel yang dioptimakan telah digunakan untuk mengkaji kesan penyepuh lindapan haba pantas (RTA) keatas filem  $\text{Ge}_{1-x}\text{Sn}_x$ . Keputusan XRD dan Raman mengesahkan penambahbaikan dalam pembentukan struktur hablur dan nano hablur (NC)  $\text{Ge}_{1-x}\text{Sn}_x$  pada suhu penyepuh-lindapan pasca-buang (PDA) 400°C. Sampel sedemikian mempamerkan keamatan fonon Raman yang meningkat dan mempunyai nilai FWHM rendah ( $\sim 9.0 \text{ cm}^{-1}$ ). Keputusan menunjukkan bahawa lapisan aloi yang optima dengan kristal yang tinggi

adalah bahan yang sesuai untuk foto-pengesanan NIR (880 nm). Akhir sekali, pembentukan aloi NC  $\text{Ge}_{1-x}\text{Sn}_x$  melalui penyepuhlindapan haba yang pantas pada perikan pebagai lapisan Ge-Sn-Ge ke atas substrat Si ditunjukkan. Dapat diperhatikan bahawa campuran fasa pejal Ge-Sn berlaku pada suhu 400 °C untuk mencipta aloi  $\text{Ge}_{1-x}\text{Sn}_x$ . Sampel yang disepuh pada 400 °C menunjukkan sifat permukaan yang stabil, keamatan fonon yang tinggi dan pengasingan permukaan yang paling minimum. Pengesan foto MSM yang difabrikasikan di atas sampel ini mempamerkan puncak sambutan di rantau NIR (820 nm). Keputusan yang telah diperolehi menunjukkan sampel amorfos and nanohablur  $\text{Ge}_{1-x}\text{Sn}_x$  sesuai menghasilkan bahan yang sesuai untuk aplikasi fotonik dan pengesan cahaya.



# **GeSn FILM DEPOSITED BY RF MAGNETRON SPUTTERING FOR PHOTODETECTOR APPLICATIONS**

## **ABSTRACT**

In this thesis, the  $\text{Ge}_{1-x}\text{Sn}_x$  semiconductor alloy films have been prepared through RF magnetron sputtering to grow the film at low temperature to suppress the Sn surface segregation. The structural, optical, electrical properties of the grown  $\text{Ge}_{1-x}\text{Sn}_x$  alloy films on silicon (Si) substrate were investigated for optoelectronic applications. The studies have been divided into three parts. The first part of this research focused on the effect of post-deposition annealing (PDA) to optimize the annealing temperature for enhancing the optical and electrical properties of room temperature sputtered  $\text{Ge}_{1-x}\text{Sn}_x$  alloy film on Si (100) substrate. The optimized  $\text{Ge}_{1-x}\text{Sn}_x$  sample at low annealing temperature of 200 °C showed higher phonon intensity, lowest surface roughness, and good electrical performance. It was observed that the optical band gap of the  $\text{Ge}_{1-x}\text{Sn}_x$  films ( $0.9 \text{ eV} < E_g < 1.05 \text{ eV}$ ) was decreased by increasing the Sn content in  $\text{Ge}_{1-x}\text{Sn}_x$  films on glass substrate, which shifts the operating wavelength to near-infrared (NIR) region. For the fabricated MSM photodetector on 200 °C annealed sample, the enhancement was obviously illustrated by improvement in the current gain and Schottky barrier height. In the second part of this research, the  $\text{Ge}_{1-x}\text{Sn}_x$  thin films were co-sputtered at various substrate temperature ( $T_s$ ). The deposited  $\text{Ge}_{1-x}\text{Sn}_x$  film at  $T_s=140$  °C exhibited crystalline phase formation with (111) orientation. This optimized sample was used to investigate the effect of rapid thermal annealing (RTA) on  $\text{Ge}_{1-x}\text{Sn}_x$  film. The XRD and Raman results confirmed the enhancement in crystalline structure and nanocrystalline (NC)  $\text{Ge}_{1-x}\text{Sn}_x$  formation at the low post-deposition annealing of 400

°C. The RTA annealed sample exhibits improved Raman phonon intensity and lower FWHM value ( $\sim 9.03 \text{ cm}^{-1}$ ). The results showed that the optimized alloy film (400 °C) with high crystallinity is appropriate material for NIR photodetection (880 nm). Finally, the NC  $\text{Ge}_{1-x}\text{Sn}_x$  alloy formation through rapid thermal annealing of multilayer sputtered Ge-Sn-Ge on Si substrate has been presented. It was observed that Ge-Sn solid phase mixing has been occurred at the low temperature of 400 °C, which results  $\text{Ge}_{1-x}\text{Sn}_x$  alloy formation. The sample anneal at the 400 °C exhibited stable morphology, high phonon intensity and less Sn surface segregation. Indeed, the fabricated MSM PD on the 400 °C annealed sample showed the responsivity peak at NIR region (820 nm). The obtained results showed that the optimized amorphous and nanocrystalline  $\text{Ge}_{1-x}\text{Sn}_x$ , which are obtained using the sputtering technique and post-deposition annealing are suitable material for photonic and light sensing device applications.

## CHAPTER 1

### INTRODUCTION

#### 1.1 Introduction

Semiconductor alloys have fascinated considerable attention as the crystalline and amorphous material in semiconductor industry [1]. In metals or ceramics, the alloying is primarily aimed at engineering mechanical behavior. However, semiconductor alloys concern achieving specific optical or electronic properties. Importantly, alloys formation is the main part in engineering semiconductors. Alloying semiconductors, in general, affects the energy band structure and minimum energy gap, lattice parameter, mechanical constants (including elastic moduli, defect formation energies, etc.), optical and electronic conduction properties, and many other aspects of the resulting material. The semiconductor alloys have been used in heterojunction bipolar transistors, laser diodes, and numerous other devices.

Silicon (Si) has been the dominant semiconductor material for about few decades. The introduction of  $\text{Ge}_{1-x}\text{Si}_x$  alloys has extended the dominance of Si technology into areas previously dominated by III-V materials [2]. However, Si, Ge and  $\text{Ge}_{1-x}\text{Si}_x$  are indirect band gap semiconductors and therefore cannot be used to fabricate laser, since it requires a direct band gap material. Now, III-V materials have played crucial rule in the field of optoelectronic devices. Crystalline  $\text{Ge}_{1-x}\text{Sn}_x$  alloys have been grown by researchers at Arizona State University, which are predicted to be a potential direct band gap material [3, 4] and most importantly can be grown on Si substrate. These materials provide an exciting and challenging platform to do science.  $\text{Ge}_{1-x}\text{Sn}_x$  is predicted to exhibit a direct band gap in unstrained alloys. Its energy band gap is tunable from 0.55 to 0 eV with  $x$  ranging from 0.20 to 0.65 as the

$\Gamma$ -point conduction band minimum decreases more rapidly than the L point valleys [5].

The substitution of tin (Sn) into germanium (Ge) lattice and making alloys of Ge and Sn attracted increasing attention as the only group-IV system with a predicted direct band gap. Soref and coworkers [6, 7] investigated the band gap variation in SiGe alloys with incorporation of Sn. The important prediction made by them is that direct band gap may be achieved in  $\text{Ge}_{1-x}\text{Sn}_x$  binary alloys and SiGeSn ternary alloys for some compositions of Sn. The incorporation of Sn lowers the direct and indirect absorption edges of Ge. Therefore, this material is attractive for infrared detector and photovoltaic applications that require band gaps lower than that of Ge. The  $\text{Ge}_{1-x}\text{Sn}_x$  alloys have demonstrated many interesting properties surpassing Si, such as wide range of tunable band gap.

The Ge-Sn alloy system has a great potential to achieve high crystallinity at low processing temperatures due to eutectically enhanced nucleation and growth process [8]. Semiconducting  $\text{Ge}_{1-x}\text{Sn}_x$  alloy, because of tunable band gap [9] and possibility of high electron and hole mobility [10] offers exciting avenues for band gap and strain engineering in a silicon compatible technology [11].  $\text{Ge}_{1-x}\text{Sn}_x$  alloy could be viable candidate as high mobility complementary metal-oxide-semiconductor (CMOS) channel and for optoelectronic devices. In the researches led by Roucka et al [12] and Xie et al [13],  $\text{Ge}_{1-x}\text{Sn}_x$  alloy exhibited higher mobility for holes and electrons than Ge. Additionally to improve carrier mobilities,  $\text{Ge}_{1-x}\text{Sn}_x$  alloy exhibits increased infrared optical absorption than Si and Ge [14], which makes it much better suited for optoelectronic applications. By Sn incorporation into Ge, the flattening of the conduction and valence band dispersion relations increase the joint density of electronic states and should lead to enhanced absorption [14]. Therefore,

thin  $\text{Ge}_{1-x}\text{Sn}_x$  films are interesting for fast photodetectors and modulators on Si CMOS for optical interconnections [15].

The epitaxial growth and synthesis of  $\text{Ge}_{1-x}\text{Sn}_x$  alloy is very challenging. First, Sn tends to segregate to the thin film surface [16]. Secondly, the equilibrium solid solubility of Sn in Ge is rather low ( $x < 0.01$ ) [17]. Finally, there is a large lattice mismatch (14.7%) between  $\alpha$ -Sn and Ge. In addition, the lattice mismatch for a  $\text{Ge}_{1-x}\text{Sn}_x$  alloy on Si (100) substrate is large (4.2-19%), which makes it hard to grow coherent epitaxial layer [18]. Despite these difficulties, this alloy can be grown in non-equilibrium growth systems like molecular beam epitaxy (MBE) [19], chemical vapor deposition (CVD) [20], pulsed laser deposition [21], solid phase crystallization [22] and sputtering [23]. Among deposition methods, magnetron sputtering is a suitable and low-cost technique for growing  $\text{Ge}_{1-x}\text{Sn}_x$  alloy films [24]. Sputtering techniques allow us to easily control the deposition parameters, such as gas flow, substrate temperature, sputtering power, alloy composition, and deposition time.

Owing to the development of Si-transistor technology beyond the 10 nm node, the researchers are looking for high mobility materials as the transistor channel to replace with Si. Germanium and  $\text{Ge}_{1-x}\text{Sn}_x$  alloy have emerged as strong contenders for the next generation of CMOS transistors [25]. It is believed that  $\text{Ge}_{1-x}\text{Sn}_x$  films may become one of the most important materials in the next generation of infrared detector and terahertz modulator, with the continuous improvement of  $\text{Ge}_{1-x}\text{Sn}_x$  film synthesis, optimization of growth parameters, improvement of heat treatment technology, and regulation of the Sn content levels [26].

## 1.2 Problem Statement

Often, in most of the researches on  $\text{Ge}_{1-x}\text{Sn}_x$  growth, the following three items are mentioned as the main challenges: the large lattice mismatch between  $\alpha$ -Sn and Ge, low equilibrium solid solubility and Sn segregation phenomena. For tackling problems aforementioned, virtual substrates is used to solve the problem of high lattice mismatch between Si and  $\text{Ge}_{1-x}\text{Sn}_x$  [27, 28]. For the low equilibrium solid solubility,  $\text{Ge}_{1-x}\text{Sn}_x$  solid solutions with a few percent Sn content can only be grown under non-equilibrium conditions, which the groups of Zaima and Kouvetakis [13, 28-30] developed specific MBE and CVD techniques, respectively. To suppress the Sn surface segregation, which is dependent on the growth temperature [31], the GeSn alloys need to grow at low temperature.

However, Sn surface segregation is still a major challenge in  $\text{Ge}_{1-x}\text{Sn}_x$  alloy growth. Increases in growth temperature lead to Sn segregation and the low growth temperatures tend to favor excess point defect levels or even a breakdown of crystalline growth into an amorphous one [32]. Many researches have been focused to optimize the growth temperature. Although methods such as MBE and CVD have been proven to form good crystalline  $\text{Ge}_{1-x}\text{Sn}_x$  alloys [33, 34], the misfit dislocations and Sn surface segregation have never quite been solved [35]. Indeed, the strict growth conditions of CVD and MBE limit the application in mass production. Magnetron sputtering presents one of the cost-effective mass manufacturing methods. Indeed, magnetron sputtering has also been used to grow  $\text{Ge}_{1-x}\text{Sn}_x$  alloy using high quality buffer layer [36], which requires high temperature growth. However, even without a buffer layer, poly- $\text{Ge}_{1-x}\text{Sn}_x$  domains were obtained on the Si substrate. Therefore, in this study, the  $\text{Ge}_{1-x}\text{Sn}_x$  alloy films have been sputtered on Si substrate without buffer layer at various elevated substrate temperature to optimize

the deposition temperature. It is considered that low-temperature growth is needed to suppress the segregation and more Sn addition to germanium. The results show that at lower elevated substrate temperature, the Sn surface segregation is less and the grown nanocrystalline  $\text{Ge}_{1-x}\text{Sn}_x$  layer is enhanced upon thermal annealing.

In addition, solid-phase techniques, which means crystallization of amorphous material, are expected to be useful to achieve a high concentration of substitutional Sn. This is because migration of atoms during growth is suppressed in solid phase methods compared with that in other approaches such as vapor-phase techniques (CVD and MBE) and liquid-phase techniques [37]. Therefore, in this work, the sputtered  $\text{Ge}_{1-x}\text{Sn}_x$  layers and multilayer Ge-Sn-Ge were undergone post-deposition annealing. The results show the enhancement in the crystalline state of RT sputtered layers and creation of  $\text{Ge}_{1-x}\text{Sn}_x$  alloy upon RTA annealing of multilayered Ge-Sn-Ge structure on Si substrate.

### 1.3 Research Objectives

The main objectives of this thesis can be summarized in the following points:

1. To investigate the deposition of amorphous  $\text{Ge}_{1-x}\text{Sn}_x$  on Si substrate using RF magnetron co-sputtering at room temperature (RT).
2. To investigate the deposition of nanocrystalline  $\text{Ge}_{1-x}\text{Sn}_x$  on Si substrate using RF magnetron co-sputtering at elevated temperature.
3. To investigate the growth of nanocrystalline  $\text{Ge}_{1-x}\text{Sn}_x$  from sputtered Ge-Sn-Ge on Si substrate.
4. To investigate the characteristics of amorphous and nanocrystalline  $\text{Ge}_{1-x}\text{Sn}_x$  MSM photodetectors.

#### 1.4 Scope of Study

This study focuses on the optimization of the room temperature sputtered  $\text{Ge}_{1-x}\text{Sn}_x$  alloy through PDA to produce high performance amorphous films. Besides, the deposition temperature of RF magnetron sputtered germanium-tin alloy film were optimized to produce nanocrystalline  $\text{Ge}_{1-x}\text{Sn}_x$  alloy on Si substrate. The amorphous and nanocrystalline materials were used to fabricate photodetectors with enhanced performance.

#### 1.5 Outline of Thesis

The reminder of this thesis is organized in the following manner, which are shortly described below.

The next chapter serves as some theories and literature review about the work.  $\text{Ge}_{1-x}\text{Sn}_x$  optical and electrical properties and its deposition were explained. In addition, the physical vapor deposition and post-deposition heat treatment were explained. At the end of the chapter some theoretical description of photodetectors and metal-semiconductor-metal (MSM) photodetectors (PDs) were given.

The experimental procedure of the related work is given in chapter 3. Here the film deposition methods are described. This included the physical deposition methods, thermal evaporation and RF sputtering. The next part of this chapter explains the instruments used in this work.

Chapter 4 discusses the results on the growth and characterization of amorphous  $\text{Ge}_{1-x}\text{Sn}_x$  thin films on Si substrate and its application in MSM PDs.

Chapter 5 discusses the results on the effect of RTA on the co-sputtered  $\text{Ge}_{1-x}\text{Sn}_x$  films on Si substrate.



Chapter 6 discusses the results of the effect of RTA on the multilayer Ge-Sn-Ge on Si substrate in order to produce  $\text{Ge}_{1-x}\text{Sn}_x$  alloy.

Finally, the thesis conclusion and discussion are given in chapter 7. Conclusion presented in this chapter, gives a brief overview of the research and the achieved results also the future works suggests a perspective of the future researches that can be implemented based on the outcomes of this thesis.

## CHAPTER 2

### LITERATURE REVIEW AND THEORY

#### 2.1 Introduction

This chapter presents literature review and the principle theories of all subjects involved in this research work. The fundamentals and growth methods of  $\text{Ge}_{1-x}\text{Sn}_x$  alloy will be described. The sputtering technique as one of the physical vapour deposition method for semiconductor thin film deposition will be explained. Afterward, the RTA process will be described, which consists of thermal furnace annealing and RTA. Finally, the fundamental and principle of semiconductor PD will be described.

#### 2.2 Fundamentals of Germanium Tin Alloy

The Ge-Sn alloy system has a great potential to achieve high crystallinity at low processing temperatures due to eutectically enhanced nucleation and growth process [8]. The equilibrium eutectic phase diagram of Ge-Sn is displayed in Fig. 2.1 [38], where the eutectic temperature is 504.1 K (231.0 °C) and the equilibrium solubility of Sn in Ge is ~1 at.% from 500 to 800 K (227 to 527 °C).

From the phase diagram, one sees the problems of equilibrium growth of  $\text{Ge}_{1-x}\text{Sn}_x$ . Sn has a low melting point (about 231.0 °C). That means at growth temperatures above 231.0 °C a two phase mixture is created; solid Ge (diamond lattice with very small Sn amount, < 1 %) and liquid Sn. Below 231.0 °C a two phase solid mixture is created, again with diamond lattice Ge (small Sn amount) and body centered cubic (metallic) Sn. A single phase is created only at the end points, either with very small Sn amount (<1%) or with very high Sn amount (>99%).

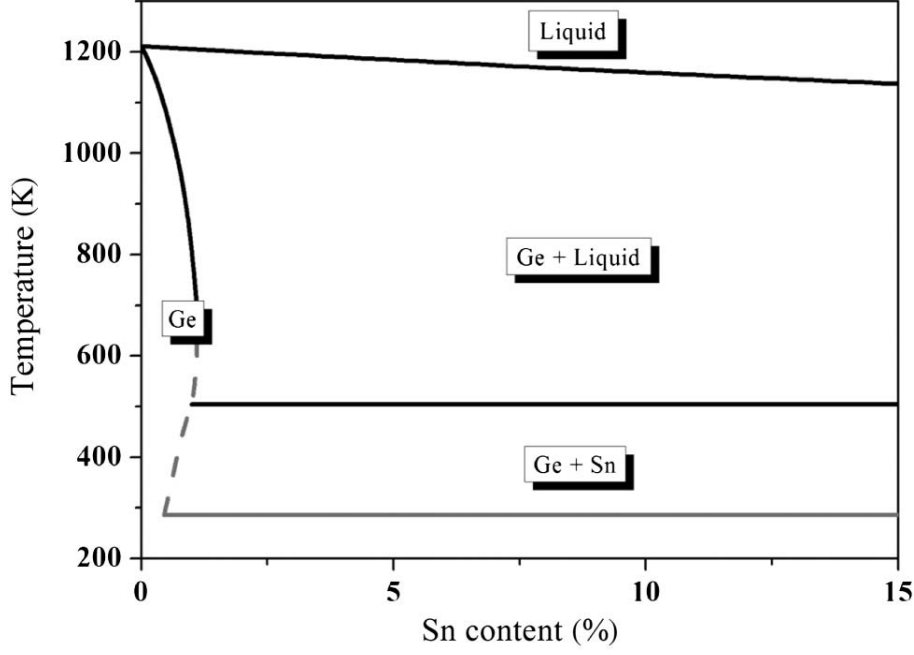


Figure 2.1. Equilibrium phase diagram of Ge-Sn. Shown is the Ge rich side up to 15% Sn [38].

There is small energy separation of 140 meV between the absolute conduction band minimum at the L-point of the Brillouin zone ( $E_{cL}$ ) and local minimum at the  $\Gamma$ -point ( $E_{c\Gamma}$ ). This energy separation can be overcome by Sn alloying. In  $\text{Ge}_{1-x}\text{Sn}_x$  alloys, incorporation of Sn content into Ge induces a lowering of energy of the conduction band at the  $\Gamma$  point [39, 40], resulting indirect-to-direct band gap transition, as shown in Fig. 2.2.

It was reported that  $\text{Ge}_{1-x}\text{Sn}_x$  alloy achieves a direct band gap structure with a Sn composition up to 8% to 11% [41-45]. Figure 2.3 displays the compositional dependence of the direct and indirect band gaps of unstrained  $\text{Ge}_x\text{Sn}_{1-x}$  alloys at room temperature. As the  $\alpha$ -Sn (Gray Tin) composition increases in the  $\text{Ge}_x\text{Sn}_{1-x}$  alloys, both the direct and indirect band gaps decrease. Grey tin ( $\alpha$ -Sn) is a semimetal with the overlap between the conduction and valence bands estimated at 0.4 eV [46]. However, the direct band gap decreases more rapidly than the indirect one due to the negative direct band gap of  $\alpha$ -Sn and the huge bowing parameter of  $\text{Ge}_x\text{Sn}_{1-x}$  alloys.

In another study, the indirect-to-direct band gap transition occurs at an  $\alpha$ -Sn mole fraction of 10.55%, which agrees well with the experimental observations [47, 48].

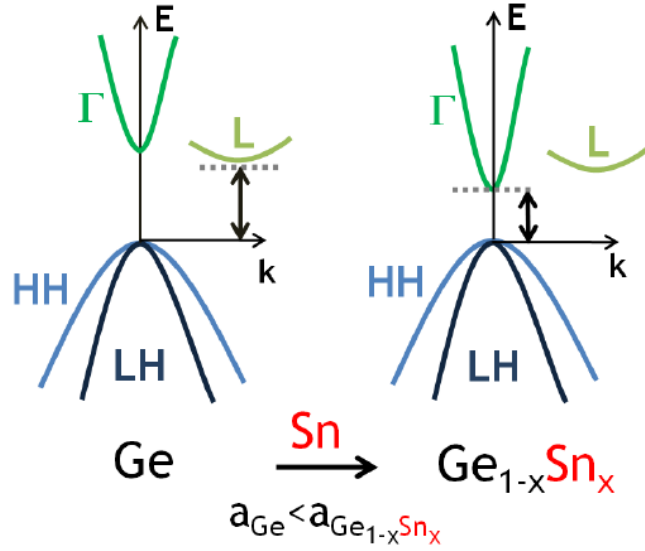


Figure 2.2. The energy separation between the L-point of the Brillouin zone ( $E_{cl}$ ) and local minimum at the  $\Gamma$ -point ( $E_{cr}$ ) [49].

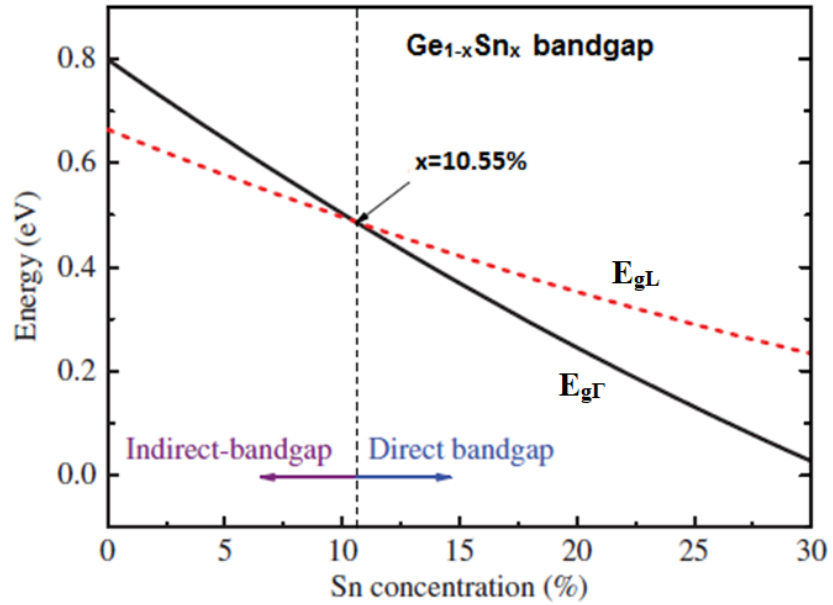


Figure 2.3. Direct and indirect band gaps of unstrained  $\text{Ge}_{1-x}\text{Sn}_x$  alloys as a function of  $\alpha$ -Sn concentration [50].

In addition, the  $\text{Ge}_{1-x}\text{Sn}_x$  alloys are expected to exhibit higher electron [51] and hole mobilities [10, 45] compared with Ge, since it is a mixed crystal of Ge and Sn whose effective mass is smaller than Ge (Table 2.1). Moreover, it was theoretically predicted that  $\text{Ge}_{1-x}\text{Sn}_x$  and strained-  $\text{Ge}_{1-x}\text{Sn}_x$  have extremely high carrier mobilities in excess of  $10^5 \text{ cm}^2/\text{Vs}$ , which makes  $\text{Ge}_{1-x}\text{Sn}_x$  as a good candidate for high-speed electronic devices [10]. The direct gap  $\text{Ge}_{1-x}\text{Sn}_x$  also increases the electrons population in the C valley with high electron mobility [45].

Table 2.1. Electron and hole mobility of group IV semiconductors.

Semiconductor	Electron mobility ( $\text{cm}^2/(\text{Vs})$ )	Hole mobility ( $\text{cm}^2/(\text{Vs})$ )
Si <sup>a</sup>	1350	480
Si (Strained) <sup>a</sup>	2300	3600
Si <sub>0.8</sub> Ge <sub>0.2</sub> <sup>a</sup>	500	250
Si <sub>0.8</sub> Ge <sub>0.2</sub> (w/o alloy scattering) <sup>a</sup>	1000	1000
Ge <sup>a</sup>	3600	1800
Sn	2500	2400
GeSn <sup>a</sup>	$10^6$	4500

<sup>a</sup>Data from Ref. [10].

In addition to improve carrier mobilities,  $\text{Ge}_{1-x}\text{Sn}_x$  shows increased optical absorption, which makes it much better suited for optoelectronic applications than Si and Ge [46, 52]. It was already demonstrated that the addition of Ge into amorphous Si reduces the band gap [53] and enhances the optical absorption at longer wavelength [54]. However, due to the critical thickness of  $\text{Si}_{1-x}\text{Ge}_x$  on Si substrate, the interesting alternative could be the germanium-tin ( $\text{Ge}_{1-x}\text{Sn}_x$ ) alloy [44, 55], which showed more optical absorption compared to pure Ge (Fig. 2.4). Therefore, thin  $\text{Ge}_{1-x}\text{Sn}_x$  layers has more potential than Si and Ge to be used for optoelectronic

applications [46, 52], such as fast photodetectors and modulators on Si CMOS for optical interconnections.

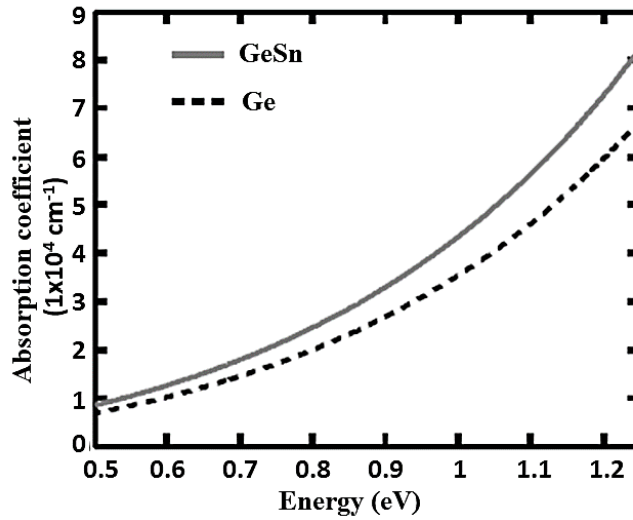


Figure 2.4. Absorption coefficient of  $\text{Ge}_{1-x}\text{Sn}_x$  with 4.5% Sn and Ge formed by solid phase epitaxy on silicon, measured by spectroscopic ellipsometry [15].

### 2.2.1 Alloy Formation Mechanism

An alloy in which atoms of one element are substituted for atoms of another element is called a substitutional alloys. Elements that can form substitutional alloys have atoms with atomic radii that differ by no more than about 15%. When one element is much smaller than another atom, they cannot substitute in the crystal lattice. This is called an interstitial alloy. For two elements to form an interstitial alloy, the atomic radius of the solute element must be less than about 60% of the atomic radius of the host metal.

The mechanism of a mass transport by atomic motion from lattice site to lattice site is called diffusion. In solids, it occurs as vacancy diffusion or interstitial diffusion (Figure 2.5). The vacancy diffusion consists of inter-diffusion and self-diffusion. In inter-diffusion in an alloy, atoms tend to migrate from regions of high concentration to regions of low concentration. Self-diffusion is occurred in elemental

solids. In vacancy diffusion, the atoms exchange with vacancies and it applies to substitutional impurities atoms. Diffusion is occurred in presence of an empty adjacent site. In addition, the atom must have sufficient energy to break bonds with its neighbor atoms. In interstitial diffusion, smaller atoms can diffuse between atoms [56].

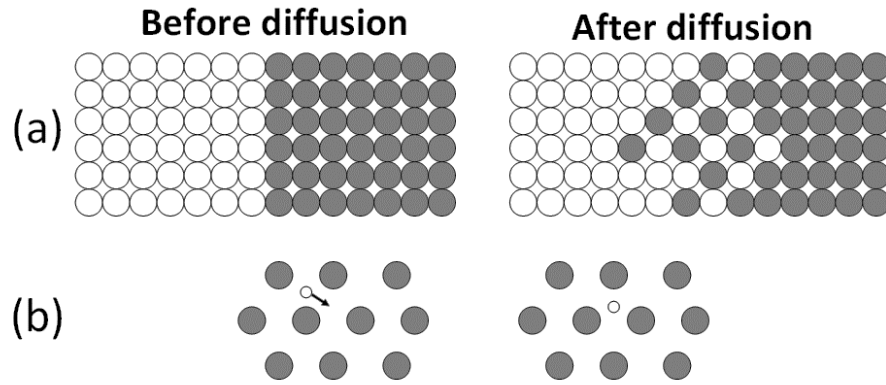


Figure 2.5. (a) Vacancy diffusion, and (b) interstitial diffusion [57].

To grow  $\text{Ge}_{1-x}\text{Sn}_x$  alloy, the Sn must be positioned in substitutional sites in crystal lattice [37]. At very low temperature growth, when the Sn adatoms cannot find the lattice positions, point defects are created as vacancies or interstitials [32]. The post-annealing prevents and reduces the Sn migration to interstitial sites [56].

### 2.3 Overview and Background of $\text{Ge}_{1-x}\text{Sn}_x$ Growth Techniques

The epitaxial growth of  $\text{Ge}_{1-x}\text{Sn}_x$  alloy is very difficult. Firstly, Sn tends to segregate to the surface [16]. Secondly, the equilibrium solid solubility of Sn in Ge is rather low ( $x < 0.01$ ) [17]. Thirdly, there is a large lattice mismatch (14.7%) between  $\alpha\text{-Sn}$  ( $a_{\text{Sn}}=6.4892 \text{ \AA}$ ) and Ge ( $a_{\text{Ge}}=5.6579 \text{ \AA}$ ) [18]. Covalent radii of Sn and Ge is  $1.22 \text{ \AA}$  and  $1.40 \text{ \AA}$ , respectively [58]. In fact, Sn precipitations in  $\text{Ge}_{1-x}\text{Sn}_x$  alloy

during epitaxial growth and annealing after growth were often found [59-61]. Conventional growth techniques working under thermodynamic equilibrium are thus not suitable for the fabrication of the metastable  $\alpha$ - $\text{Ge}_{1-x}\text{Sn}_x$  alloys.  $\alpha$ -Sn (nonmetallic form, or gray tin), which is stable below 13.2 °C, is brittle and has a diamond cubic crystal structure, similar to diamond, silicon or germanium.

Despite these difficulties, significant efforts have been made in growing  $\text{Ge}_{1-x}\text{Sn}_x$  alloys using physical and chemical growth techniques by MBE [19, 62], ultra-high vacuum chemical vapor deposition (UHV-CVD) [20], pulsed laser deposition [21], solid phase crystallization [22], and sputtering [23].

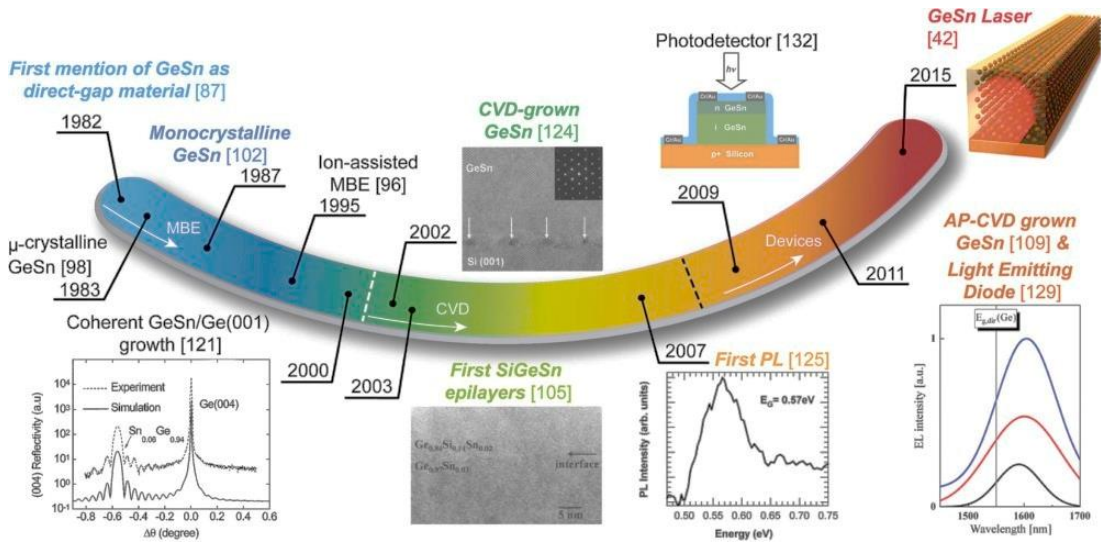


Figure 2.6. Timeline of  $\text{Ge}_{1-x}\text{Sn}_x$  epitaxy providing an overview of important achievements since  $\text{Ge}_{1-x}\text{Sn}_x$  has been mentioned for the first time as possible direct band gap material in 1982 [63, 64].

Figure 2.6 shows the most important achievements of Si-Ge-Sn epitaxy, which displayed in a brief timeline. After proposing the  $\text{Ge}_{1-x}\text{Sn}_x$  alloy in 1982 by Soref et al., for the first time in 1983, thin microcrystalline films of metastable semiconducting alloy  $\text{Ge}_{1-x}\text{Sn}_x$  have been formed using excimer laser radiation to



crystallize amorphous sputtered films on glass and semiconducting crystalline substrates [65]. In 1987, monocrystalline metastable  $\text{Ge}_{1-x}\text{Sn}_x$  has been grown using bias-sputter deposition on Ge(100) and GaAs(100) substrates [66]. In 1995,  $\text{Ge}_{1-x}\text{Sn}_x$  has been synthesized using ion-assisted MBE [67]. In 2004,  $\text{Ge}_{1-x}\text{Sn}_x$  alloy has been grown on Si(100) substrate using UHV-CVD and the results exhibited superior crystallinity and thermal stability compared with MBE grown films [68]. In addition,  $\text{Si}_{1-x-y}\text{Ge}_x\text{Sn}_y$  which is another ternary semiconductor alloy from IV group has been synthesis via UHV-CVD [69].

### 2.3.1 CVD

Chemical vapor deposition (CVD) involves the formation of a thin solid film on a substrate material by a chemical reaction of vapour-phase precursors. The chemical reactions of precursor species occur both in the gas phase and on the substrate. Reactions can be promoted or initiated by heat (thermal CVD), higher frequency radiation such as ultra violet (UV) (photo-assisted CVD) or a plasma (plasma-enhanced CVD). In chemical vapor deposition, the deposition of a thin film is initiated and driven by chemical reactions between gaseous reactants (precursor) consisting inter alia of atoms of the final layer material - and the substrate. This deposition technique allows cost effective and large-scale fabrication of monocrystalline, amorphous and polycrystalline layers.

The first CVD-grown  $\text{Ge}_{1-x}\text{Sn}_x$  epilayers introduced by the group of Taraci et al. [68, 70], which uses mixtures of digermane ( $\text{Ge}_2\text{H}_6$ ) and deuterated stannane ( $\text{SnD}_4$ ), is particularly attractive for its simplicity and compatibility with silicon technology. In addition, this group published the first photoluminescence results on the  $\text{Ge}_{1-x}\text{Sn}_x$  alloy in 2007 [71]. Furthermore, Vincent et al. [72] succeeded in growing high-

quality  $\text{Ge}_{0.92}\text{Sn}_{0.08}$  epilayers in 2011 using atmospheric pressure CVD and commercially available precursors such as digermane ( $\text{Ge}_2\text{H}_6$ ) along with tin chloride ( $\text{SnCl}_4$ ).

The development of CVD techniques resulted in fabrication of various applications of  $\text{Ge}_{1-x}\text{Sn}_x$ , e.g. photodiode [73-75], light emitting diodes (LEDs) [76], photodetectors [77-79] and MOSFETs [80].

### **2.3.2 MBE**

Molecular beam epitaxy (MBE) is a versatile method for growing thin epitaxial films made of variety of semiconductors, metals or insulators. It was first applied to the growth of compound semiconductors. That is still the most common usage, in large part because of the high technological value of such materials to the electronics industry. This technique has significantly more precise control of the beam fluxes and growth conditions. Due to the vacuum deposition, MBE is carried out under conditions far from thermodynamic equilibrium, which is suitable for growing  $\text{Ge}_{1-x}\text{Sn}_x$  alloy. The deposition process in MBE is governed mainly by the kinetics of the surface processes occurring when the impinging beams react with the outermost atomic layers of the substrate crystal. This is in contrast to other epitaxial growth techniques, such as liquid phase epitaxy (LPE) or atmospheric pressure vapor phase epitaxy (VPE), which proceed at conditions near thermodynamic equilibrium and are most frequently controlled by diffusion processes occurring in the crystallizing phase surrounding the substrate crystal [81].

As mentioned earlier, the  $\text{Ge}_{1-x}\text{Sn}_x$  alloy was grown using MBE by many researchers. In this method, Ge and Sn were simultaneously deposited using Knudsen

cells under ultra-high vacuum condition. The growth temperature was 150 or 200 °C to suppress Sn precipitation [82].

### 2.3.3 Sputtering

Sputtering is one of the processes for depositing thin films on suitable substrates and is widely used for preparing metals, insulators, and amorphous and crystal semiconductor films. The source material for sputter deposition of thin films is called the sputtering target. In sputtering process, atoms are ejected from a target material by using energetic particles inside a chamber [83]. In principle, the majority of solid materials can be sputtered under suitable conditions to form thin films.

Combining the advantages of the MBE and CVD methods, the sputter approach used for  $\text{Ge}_{1-x}\text{Sn}_x$  growth is non-toxic and feasible for mass production. This is of great interest for  $\text{Ge}_{1-x}\text{Sn}_x$  applications if high-quality  $\text{Ge}_{1-x}\text{Sn}_x$  films can be grown by sputtering.

The first monocrystalline and single phase  $\text{Ge}_{1-x}\text{Sn}_x$  epilayers have been grown by Shah et al. [84] via bias sputtering deposition on Ge(100) and GaAs(100) substrates. Whereas diamond structure polycrystalline  $\text{Ge}_{1-x}\text{Sn}_x$  have been obtained for Sn concentrations up to 15 at. %, while a maximum Sn content of 8 at.% has been achieved in single crystal layers.

Although many researches have been carried out on  $\text{Ge}_{1-x}\text{Sn}_x$  growing by sputtering technique, there are limited studies on the crystalline growth of this alloy, compared to other deposition techniques such as MBE and CVD. In the study led by Tsukamoto [24], the crystalline  $\text{Ge}_{1-x}\text{Sn}_x$  alloy with a Sn content up to 11.4% has been grown by sputtering. However, the surface segregation of Sn was observed in the grown  $\text{Ge}_{1-x}\text{Sn}_x$  layers at growth temperatures of 548 K (311 °C) and above,

which increases the surface roughness. In another study [36], crystalline  $\text{Ge}_{1-x}\text{Sn}_x$  films were successfully grown on Si (100) substrates by low-temperature magnetron sputtering at 150 °C. In addition, they demonstrated that  $\text{Ge}_{1-x}\text{Sn}_x$  films grown by sputtering appear to have great promise for the cost-effective fabrication of Si-based infrared devices. Moreover, the ternary alloy  $\text{Ge}_{1-x-y}\text{Si}_x\text{Sn}_y$  has been grown on Ge-buffered Si (100) substrate by magnetron sputtering [85]. It was demonstrated that the  $\text{Ge}_{1-x-y}\text{Si}_x\text{Sn}_y$  can maintain good crystalline quality under moderate annealing temperature, with no indication of phase segregation or Sn precipitation. In [86], the DC magnetron sputtering was used to grow  $\text{Ge}_{1-x}\text{Sn}_x$  at a temperature of 250 °C. In this study [86], the Ge buffer layer has been used to reduce the stress by  $\text{Ge}_{1-x}\text{Sn}_x$  onto the Si substrate. In general, all the researches aim to sputter  $\text{Ge}_{1-x}\text{Sn}_x$  alloy film at low temperature, to suppress the Sn surface segregation and to incorporate more Sn in germanium.

#### 2.3.4 Laser Synthesis

Laser crystallization process induces crystallinity, whereby the material's properties can be precisely controlled. In this process, an amorphous semiconductor thin film on a substrate is irradiated with a laser beam. In laser crystallization process, pulsed excimer lasers have been widely used for the mass production of poly-Si thin films at a low processing temperature. This is due to the rapid and local heating of laser, which results crystallization of silicon films with a low heating energy [87-89]. This technique is often used for making thin-film transistors that can be used for flat panel displays.

This technique is employed for crystallization of  $\text{Ge}_{1-x}\text{Sn}_x$  alloy films. Thin microcrystalline  $\text{Ge}_{1-x}\text{Sn}_x$  ( $x \approx 0.22$ ) films have been synthesized using excimer laser

radiation to crystallize amorphous sputtered films on glass and semiconducting crystalline substrates [65]. To do this, short pulse UV laser was used to anneal the thin film. In another study [90], silicon-germanium-tin microstructures has been synthesized using pulsed laser induced epitaxy for growing strained germanium (s-Ge) or  $\text{Ge}_{1-x}\text{Sn}_x$  alloys with high Sn content as a virtual substrate. In [21], heteroepitaxial  $\text{Ge}_{1-x}\text{Sn}_x$  and  $\text{Si}_{1-x-y}\text{Ge}_x\text{Sn}_y$  alloys were achieved with graded composition on Si(001) substrates using pulsed laser induced epitaxy. The transition from  $\text{Ge}_{1-x}\text{Sn}_x$  to  $\text{Si}_{1-x-y}\text{Ge}_x\text{Sn}_y$  was attained by varying the number of laser pulses accordingly with the level of intermixing between Si, Ge, and Sn. In general, the laser induced crystallization is capable to form binary and ternary alloys.

## 2.4 Semiconductor Thin Films

A thin film is a layer up to approximately 1  $\mu\text{m}$  in thickness. The thin film results from the atomic growth process and its properties are significantly different from those of the bulk material [91]. Thin film materials have been used in many semiconductor devices such as rectifiers, transistors, solar cells, light-emitting diodes, photoconductors, photodetectors, and light crystal displays. Application areas of semiconductor thin films are including electronics and optoelectronics. One of the main reason for semiconductor thin films development is to reduce the amount of light absorbing material (thickness reduction) in optoelectronic devices.

Both amorphous and crystalline thin films have immense importance in the semiconductor device technology. In the amorphous (non-crystalline) materials, the chemical bonding of atoms are approximately unchanged from crystals. The disorder variation in the atomic bond angles prevent regular lattice structure formation. One of the most important amorphous material is amorphous Si, which has been used in solar cell fabrication [92, 93].

Thin films are studied based on the optical, electrical, magnetic, chemical, mechanical, and thermal properties. There are some factors that influence the physical, electrical, optical and other properties of the thin films such as: deposition rate, substrate temperature, environmental conditions, and source material purity [94].

Thin solid film technology contains deposition of individual molecules or atoms on substrate. The thin film growth methods usually can be divided in two main categories: physical vapour deposition (PVD) and chemical deposition. In PVD process, the source material is physically converted to vapour phase. This is followed by transporting the vapour phase toward the substrate and then the vapour condenses on the substrate to create the thin films. The PVD method consists of evaporation, sputtering, and molecular beam epitaxy. Michael Faraday pioneered the first PVD process in the early 1800's [95]. It is important to mention that the development of thin films technology by PVD owed to the vacuum systems.

In chemical vapor deposition, a volatile liquid precursor produces a chemical reaction on a substrate surface, which leads to formation of a chemically deposited coating. Among chemical and electrochemical methods, the most important are chemical vapour deposition, cathode electrolytic deposition, anodic oxidation and chemical bath deposition.

#### **2.4.1 Physical Vapor Deposition**

This is a vaporization coating method, which involves transferring of material on an atomic scale under high vacuum. Unlike the CVD method, the source material is in solid form.